Lead-Free Perovskite Nanocrystals Decorating Graphene for Detecting Nerve Agents

Juan Casanova-Chafer[1,2*], Rocío Garcia-Aboal[3], Kevin Mego[3], Pedro Atienzar[3], Eduard Llobet[2]

[1] Université de Mons, Place du Parc 23, 7000 Mons, Belgium

[2] Universitat Rovira i Virgili, Països Catalans 26, 43007 Tarragona, Spain

[3] Instituto de Tecnología Química, CSIC-UPV, Universitat Politècnica de València, 46022 Valencia, Spain

*Corresponding author: juan.casanovachafer@umons.ac.be

Keywords: lead-free perovskites, graphene, DMMP, nerve agent, chemical gas sensor, resistive sensor

Abstract

Highly toxic chemical compounds known as chemical warfare agents (CWA) present substantial threats to human health and safety. Their swift detection and identification play a critical role in preventing exposure and ensuring timely intervention. This work develops nanohybrids to detect dimethyl methylphosphonate (DMMP), a simulant gas for sarin compound, which is classified as a nerve agent. Specifically, two different compositions ($Cs_3Cu_2Br_5$ and $Cs_2AgBiBr_6$) of lead-free perovskite nanocrystals (NCs) have been employed to decorate graphene. The sensitive films exhibit remarkable sensitivity to DMMP at the ppb range and under ambient temperature conditions. It is worth mentioning that this work reports for the first time the successful use of perovskite NCs for the detection of DMMP. Besides, the sensing performance of both perovskites has been compared, revealing that $Cs_3Cu_2Br_5$-decorated graphene outperforms $Cs_2AgBiBr_6$, offering up to a 4-fold improvement. The synthesis and decoration process are straightforward, industrially scalable, and inexpensive, while the use of lead-free perovskites leads to an environmentally friendly and harmless approach. These facts linked to a sensitive and reversible detection of DMMP at low concentrations pave the way for developing new CWA gas sensors based on the use of lead-free perovskite NCs.

Chemical warfare agents (CWA) have been developed as weapons of mass destruction due to their ability to inflict severe harm, and even death, upon humans [1]. Among the different types of CWAs, nerve agents are engineered to disrupt the normal functioning of the nervous system, often leading to fatal outcomes [2]. The susceptibility to exposure in the event of a chemical terrorist attack and the potential for mass casualties pose significant challenges for authorities responsible for incident prevention. Thereby, detecting nerve agents promptly becomes crucial to preventing exposure, and early warning detection systems play a crucial role in minimizing casualties, given the limited time available to perceive an attack and set alarms for evacuation.

In laboratory settings, the use of sarin gas presents substantial risks. Therefore, dimethyl methylphosphonate (DMMP), belonging to the organophosphorus compound class, serves as a widely utilized simulant for sarin gas [3]. DMMP is moderately toxic, can cause irritation to the eyes, skin, and respiratory system, along with symptoms such as nausea, vomiting, and headaches upon inhalation in substantial quantities [4]. Notably, DMMP's high volatility makes it suitable for gas-phase detection.

Different techniques have been employed to detect CWAs. For instance, gas chromatography (GC) coupled to mass spectrometry (MS) has been employed to detect and quantify DMMP accurately [5,6]. However, GC-MS presents several bottlenecks for its implementation in real-time monitoring settings. This technique requires trained personnel, it is expensive and their miniaturization for in-field measurements remains an issue [7]. Conversely, the use of chemical sensors based in different technologies such as electrochemical devices [8], acoustic wave sensors [9], colorimetric sensors [10] and semiconductors [11] have been attracted a growing research interest owing to their easy operation, cost-effectiveness and quick readouts.

Thereby, real-time monitoring of organophosphorus compounds in the atmosphere, especially in critical areas susceptible to terrorist attacks, necessitates the establishment of extended sensing networks for timely interventions. In this perspective, the implementation of such networks faces challenges, requiring low-powered, inexpensive, and accurate sensors [12]. Among the various gas sensor types, chemical resistive (chemiresistive) gas sensors have garnered significant attention due to their

high sensitivity, cost-effectiveness, ease of fabrication, real-time monitoring capabilities, and rapid detection [13,14].

Traditionally, metal oxide (MOX)-based gas sensors have been employed to detect DMMP. Various nanostructures, including SnO_2 [15], WO_3 [16], ZnO [17] and Co_3O_4 [18], have been utilized for the detection of CWAs. However, MOXs typically demand high operating temperatures (i.e., some hundreds of Celsius degrees), leading to drawbacks such as increased power consumption, reduced long-term stability, and higher costs due to the complexity of circuitry and additional elements like heaters. Alternatively, carbon-based nanomaterials have emerged as a feasible option for detecting gas compounds at ambient temperature [19]. Yet, the use of bare nanostructures, such as graphene layers, presents limitations in sensitivity compared to MOX. The primary reason is the poor specificity and reactivity of the sp^2 carbon configuration, which usually leads to poor sensing performance [20–22].

To address this limitation, a common approach involves functionalizing, decorating, or creating nanohybrids by combining carbon-based materials with other nanomaterials exhibiting higher reactivity. Some examples include graphene functionalized with organic compounds such as triphenylene [23], p-phenylenediamine [24] or cobalt phthalocyanine [25]. It is worth mentioning that combining graphene with organic compounds enable ambient or moderate working temperatures, avoiding the potential degradation issues faced by MOX-based sensors operated at elevated temperatures. Another common strategy is combining carbon-based nanomaterials with polymers. For instance, graphene can be decorated with polypyrrole (PPy) nanoparticles to effectively detect DMMP gas at ppm levels and under room temperature [26,27]. In a more advanced hybrid development, Yang and collaborators engineered a PPy-rGO composite with the introduction of Cu^{X+} ions, inducing a 4.5-fold improvement in the detection of DMMP [28].

Nevertheless, the use of halide perovskites for the detection of nerve agents remains unexplored. This work marks the first successful implementation of perovskite nanocrystals (NCs) for the detection of DMMP, a simulant for CWA. Specifically, graphene has been decorated with NCs of two compositions, $Cs_3Cu_2Br_5$ and $Cs_2AgBiBr_6$. Furthermore, the lead-free nature of these perovskites adds to their significance, considerably reducing the

hazardous nature of the sensitive film while maintaining outstanding sensing properties.

Materials and methods

Lead-free nanocrystal synthesis and graphene decoration

Two lead-free perovskite nanocrystals, $Cs_3Cu_2Br_5$, and $Cs_2AgBiBr_6$, were synthesized using hot injection methods [29,30]. In the initial step, cesium oleate was prepared by mixing 0.814 g of Cs_2CO_3, 2.5 mL of oleic acid (OA), and 40 mL of Octadecene (ODE) in a 100 mL 3-neck flask. The mixture was heated to 120 °C under vacuum for 1 hour, followed by an increase in temperature to 150 °C under a nitrogen atmosphere to completely solubilize Cs_2CO_3. The resulting Cs-oleate solution was cooled to room temperature, causing the precipitation of Cs-oleate and ODE as supernatant. In subsequent synthesis steps, the Cs-oleate solution was preheated to 100 °C before injection.

For $Cs_3Cu_2Br_5$ nanocrystals, 71 mg of $CuBr_2$ were added to 6 mL of ODE. The solution was heated at 120 °C for 1 hour under vacuum, followed by the addition of 1 mL of OA and 1 mL of dried oleylamine (OLA) under a nitrogen atmosphere. The temperature was then increased to 160°C, and 6 mL of the Cs-oleate solution was swiftly injected. After 5 seconds, the reaction mixture was rapidly cooled using an ice-water bath, leading to nanocrystal precipitation. The nanocrystals were extracted through centrifugation (6000 rpm for 5 min) and redispersed in isopropanol, resulting in a stable perovskite suspension.

For $Cs_2AgBiBr_6$ nanocrystals, $BiBr_3$ (45 mg), $AgNO_3$ (17 mg), and HBr (100 µL) were added to 4 mL of ODE. The solution was heated at 120 °C under vacuum for 1 hour, followed by further heating to 200 °C under a nitrogen flow. 0.8 mL of the Cs-oleate solution was injected, and the mixture was rapidly cooled using an ice-water bath after 5 seconds. Finally, the nanocrystals were obtained through centrifugation (7000 rpm for 10 min) and redispersed in isopropanol after multiple washing steps.

Following the perovskite synthesis, commercially available graphene nanoplatelets (Strem Chemicals Inc., US) were dispersed in isopropanol (0.3 mg/mL). Graphene was exfoliated using pulsed sonication (1s on/2s off) at 280 W for 90 minutes in an ultrasonic tip. Subsequently, $Cs_3Cu_2Br_5$ and $Cs_2AgBiBr_6$ nanocrystals (5% wt.) were added to the graphene solutions. To

achieve suitable suspension of perovskite nanocrystals on graphene, the mixtures were sonicated in an ultrasonic bath for 1 hour. The presence of defects and surface oxygenated functional groups in graphene likely facilitated non-covalent interactions with the perovskite nanocrystals, such as Van der Waals forces and hydrogen bonds [31,32].

Sensor Fabrication and Gas-Sensing Setup

The resulting graphene decorated with different lead-free perovskite nanocrystals were deposited using a spray coating technique with pure nitrogen as the carrier gas. Specifically, the hybrid nanomaterials were deposited onto interdigitated electrodes (IDE) already screen-printed on alumina substrates. The layer deposition was performed by placing the substrate on a hotplate at 85°C. The spray was generated for about 30-40 seconds until the whole electrode area was covered by the active nanomaterial. Regarding the device dimensions, the full size of the alumina substrates is 25.4 x 4.1 mm, while the electrodes comprise an area of 7.3 x 2.5 mm. Figure S1 shows images of the top and bottom sides of the substrates.

An advanced gas system was engineered to assess varying concentrations of DMMP diluted in synthetic air. This system consisted of two mass flows, both receiving synthetic air (Air Premier Purity: 99.995%) directly from a calibrated bottle. One of these mass flows was connected to a permeation system that generates DMMP gas, comprising a stainless-steel tube covered with a heated belt. The entire permeation system was linked to a PID controller (proportional integral derivative) to maintain a stable temperature inside the tube. At this line's end, another mass flow controller facilitated the dilution with the synthetic air-controlled mass flow. Additional details of the gas system setup are detailed at the supplementary information.

The internal tube of the permeation system to generate DMMP was calibrated by the customer. The gas concentration to be generated could be adjusted by regulating the system's temperature and flow. The following formula was applied to calculate the DMMP concentration generated:

$$Concentration(ppb) = 1000 \cdot Permeation\ Rate\left(\frac{ng}{min}\right) \cdot \frac{\frac{Molecular\ Volume\left(\frac{dm^3}{mol}\right)}{Molecular\ Weight\left(\frac{g}{mol}\right)}}{Sample\ Flow\left(\frac{ml}{min}\right)} \cdot \frac{Sample\ Flow\left(\frac{ml}{min}\right)}{Sample\ Flow\left(\frac{ml}{min}\right) + Split\ Flow\left(\frac{ml}{min}\right)}$$

However, it is worth noting that this work applies a constant temperature and flow through the stainless-steel tube. In that way, the reproducibility was ensured and the potential deviations in the analyte concentrations were mitigated. Alternatively, since a constant concentration of DMMP was generated, the second mass flow controller was used to apply synthetic air and dilute the DMMP until the desired concentration.

Nevertheless, to know the DMMP concentration generated, is essential to calculate the permeation rate of the analyte. This parameter can be adjusted at different temperatures as the following equation illustrates:

$$PermeationRate\left(\frac{ng}{min}\right) = 10\text{^}\left(\log e - 2950 \cdot \left(\frac{1}{Temperature\ Setpoint(℃) + 273} - \frac{1}{Calibration\ Temperature(℃) + 273}\right)\right)$$

However, since the temperature of the permeation tube was set to a constant 85 °C, the permeation rate of DMMP was 1042 ng/min. Consequently, a concentration of 2.1 ppm was constantly produced, representing the maximum concentration tested. This flow, containing this 2.1 ppm of DMMP, was subsequently diluted with synthetic dry air to achieve the desired pollutant concentrations. To ensure the precision and the reproducibility of these experimental conditions, both the temperature of the permeation tube and the overall flow rate (100 mL/min) were maintained constant. Figure S2 depicts a scheme of the gas sensing system setup.

Results and discussion

Nanomaterial Characterization

Figure 1a depicts the Raman spectrum of the bare graphene, showing prominent bands at 1345 cm^{-1} (D), 1565 cm^{-1} (G), 2690 cm^{-1} (2D). The D is indicative of structural defects such as disorder in the sp^2 carbon nanostructure, amorphous carbon, or carbonaceous impurities [33]. While the G band represents the in-plane vibrations of sp^2 carbon bonds. Finally, the 2D band is a characteristic peak related to the presence of monolayer graphene. The assessment of the D/G ratio confirms that the graphene does not present high crystallinity, due to the presence of defects and oxygen functional groups grafted on the graphene surface [34]. Nevertheless, defects and oxygen species play a crucial role in the interaction and immobilization of lead-free perovskite nanocrystals on the graphene surface [35].

The X-ray Diffraction (XRD) patterns of the perovskite NCs were recorded using a Philips X'PERT diffractometer equipped with a proportional detector and a secondary graphite monochromator. The data was registered over the range 2θ = 2–20°, with steps of 0.02°, an accumulation time of 20 s/step, and employing Cu Kα radiation (λ = 1.54178 Å). Figure 1b shows the obtained diffractograms for both NCs. A comparison with previously reported patterns [29,30,36] revealed a consistent match, confirming the orthorhombic and cubic phases for $Cs_3Cu_2Br_5$ and $Cs_2AgBiBr_6$, respectively. In addition, the obtained patterns do not show any preferential crystal orientation.

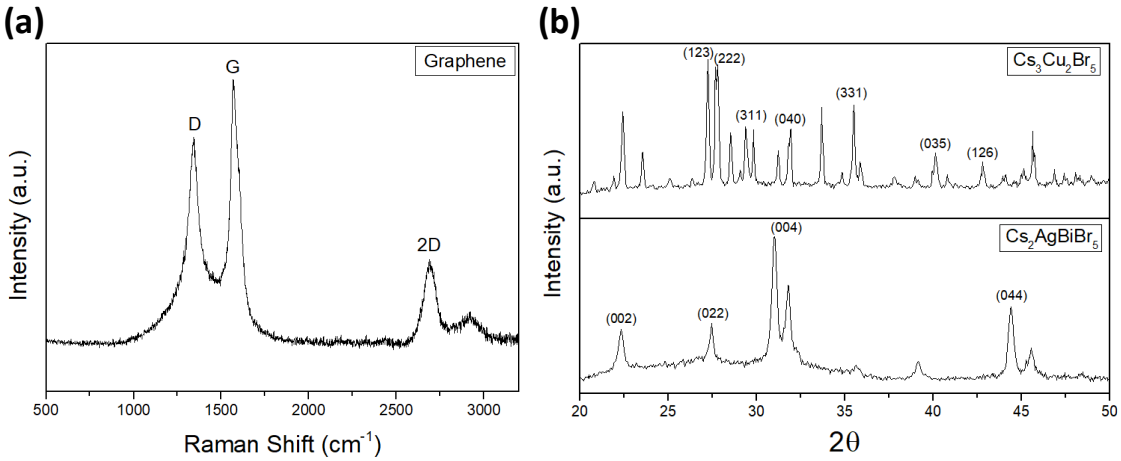

Figure 1. (**a**) Raman spectrum of bare graphene. (**b**) XRD patterns of both lead-free perovskite nanocrystals.

High-Resolution Transmission Electron Microscope (HRTEM) images were obtained using a JEOL JEM 2100F. Figure 2a and Figure 2b shows examples of both $Cs_3Cu_2Br_5$ and $Cs_2AgBiBr_6$ NCs, respectively. It is worth noting that all nanocrystals present diameters below 10 nm and both types present high crystallinity. These similar parameters facilitate a reliable comparison of sensing performance employing both NCs.

Finally, the resulting nanomaterial, comprising graphene decorated with lead-free perovskites, underwent analysis using a high-angle annular dark-field scanning transmission electron microscopy (HAADF-STEM). Figure 2c and 2d show, the $Cs_3Cu_2Br_5$ and $Cs_2AgBiBr_6$ perovskite NCs distribution on graphene. Besides, Figure S3 presents histograms of the nanocrystal size distribution, showing that both perovskites have a higher prevalence in the diameter ranging from 5 to 10 nm. Figure S4 shows a field-effect scanning electron microscope (FESEM) image, exhibiting a uniform layer of the developed nanohybrid, emphasizing the crucial porous surface for gas

sensing performance. In this regard, a previous analysis found that the graphene employed presents an extremely high BET area of 730 m^2/g [37].

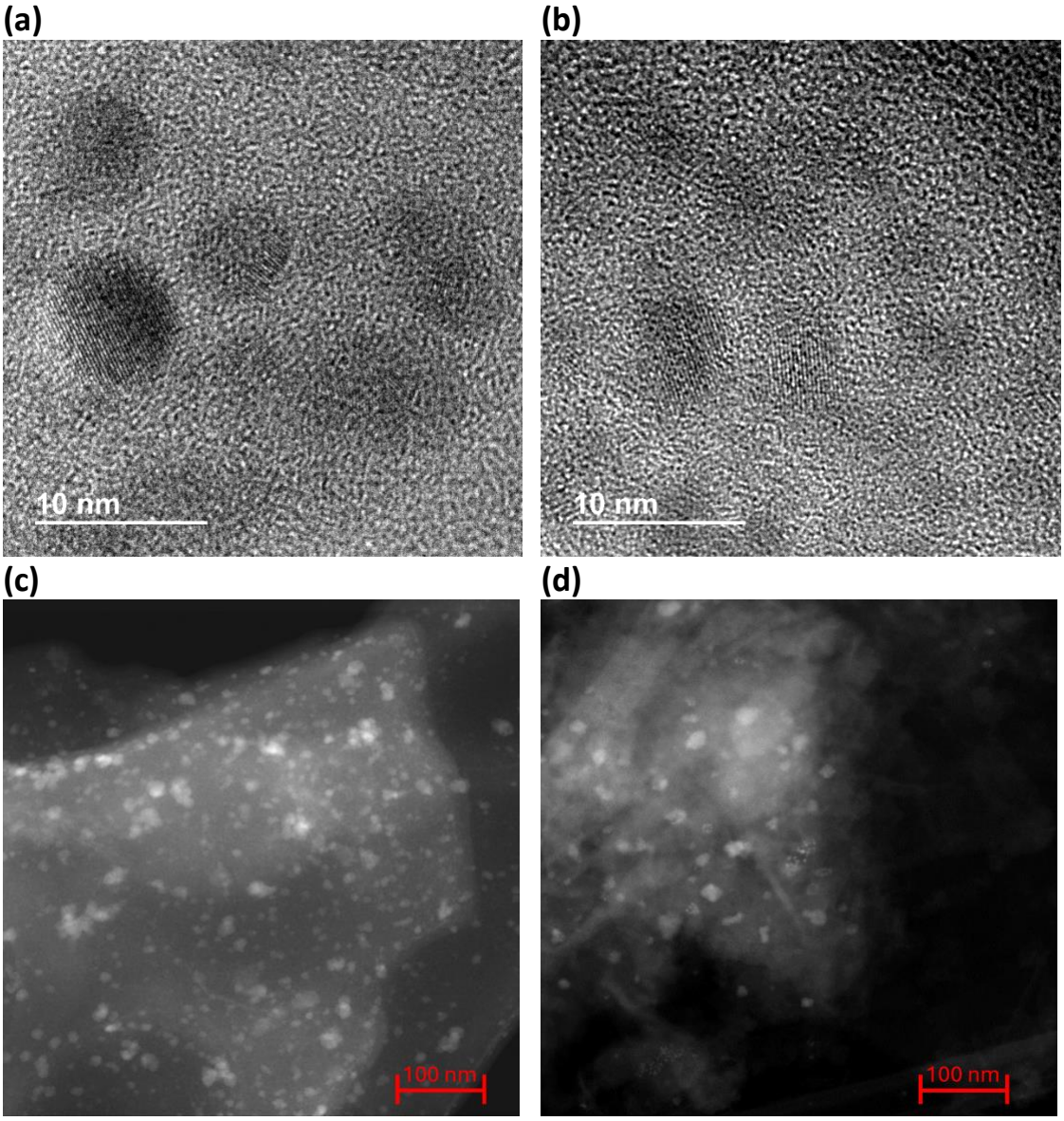

Figure 2. HRTEM images for (**a**) $Cs_3Cu_2Br_5$ and (**b**) $Cs_2AgBiBr_6$ NCs. HAADF-STEM images for (**c**) $Cs_3Cu_2Br_5$@Graphene and (**d**) $Cs_2AgBiBr_6$@Graphene. Bright spots indicate the distribution of lead-free perovskites, while the grey background corresponds to the graphene.

Gas sensing performance

The sensing performance of the lead-free perovskite NCs decorating graphene for detecting DMMP was assessed at room temperature. Various concentrations of the simulant nerve agent, ranging from 600 ppb to 2.1 ppm were applied for 5 minutes, succeeded by exposure to dry air for 15 minutes to restore the baseline resistance. Figure 3a and Figure 3b depict

the dynamic electrical responses of graphene decorated with $Cs_3Cu_2Br_5$ and $Cs_2AgBiBr_6$ nanocrystals (NCs), respectively. It is worth highlighting that both lead-free perovskites demonstrate clear resistance changes upon exposure to DMMP.

However, the dynamic responses of $Cs_3Cu_2Br_5$@Graphene present a more effective baseline recovery compared to $Cs_2AgBiBr_6$@Graphene. This observation suggests a partial reversibility in the interaction between $Cs_2AgBiBr_6$ and DMMP, leading to a linear baseline drift. In contrast, $Cs_3Cu_2Br_5$ NCs exhibit an almost complete baseline recovery after interaction with DMMP, indicating a higher degree of reversible interaction. From this perspective, $Cs_3Cu_2Br_5$ NCs likely offer superior repeatability and long-term stability compared to $Cs_2AgBiBr_6$.

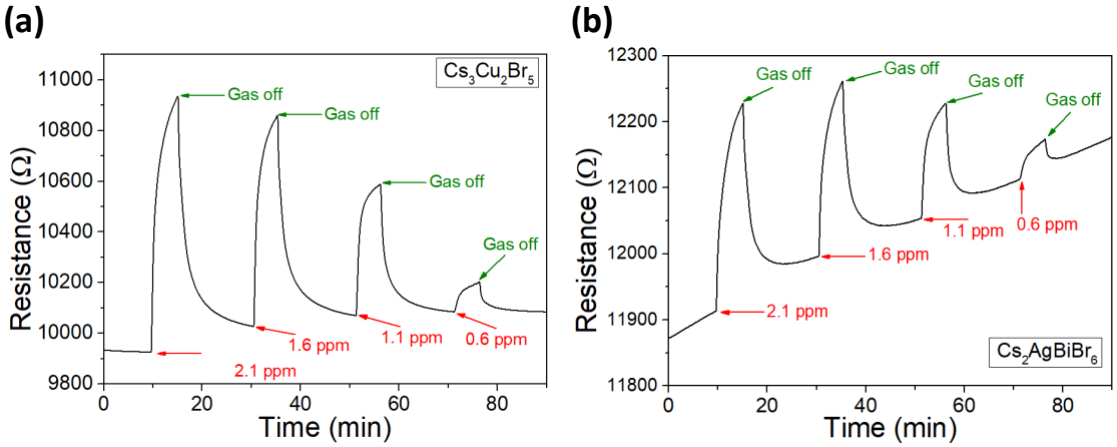

Figure 3. Electrical responses for graphene decorated with (**a**) $Cs_3Cu_2Br_5$ and (**b**) $Cs_2AgBiBr_6$ for detecting DMMP at ambient temperature.

Considering the observed resistance changes, the calibration curves for detecting DMMP at room temperature are illustrated in Figure 4. Notably, when graphene is decorated with $Cs_3Cu_2Br_5$ NCs, the responses are up to 4-fold higher compared to $Cs_2AgBiBr_6$ NCs. This substantial enhancement in the sensing performance of $Cs_3Cu_2Br_5$ is further confirmed by the sensitivity, determined by the slope of the calibration curves. In this context, the sensitivity values are 7.2% and 1.6% per ppm of DMMP for $Cs_3Cu_2Br_5$ and $Cs_2AgBiBr_6$ NCs, respectively. Additionally, bare graphene was also studied to unravel the role of the perovskite NCs. Figure S5 presents an example of the electrical responses obtained for the detection of the analyte, while Figure 4 demonstrates that the presence of perovskite NCs enhances the sensing responses. Specifically, graphene decorated with $Cs_3Cu_2Br_5$ exhibits a sensitivity of 7.2% per ppm, compared to only 0.6% per ppm for bare

graphene. This translates to a 12-fold increase in sensitivity when graphene is decorated with $Cs_3Cu_2Br_5$ compared to its bare counterpart.

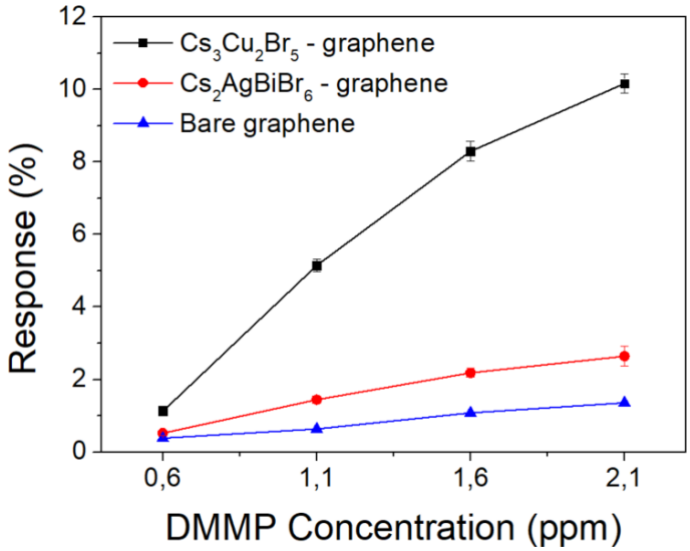

Figure 4. Calibration curves obtained for lead-free perovskite NCs decorating graphene when detecting DMMP at RT.

Table 1 summarizes the sensing performance of various graphene-based gas sensors for detecting DMMP at RT. By comparison, graphene decorated with lead-free perovskite NCs, particularly for the $Cs_3Cu_2Br_5$ NCs, has shown one of the highest sensing performances. Other experimental details should be considered besides critical parameters, such as the sensing response given by the response per unit of DMMP concentration. For instance, the flow rate is paramount since higher flow rates induce greater responses and faster baseline recovery. Conversely, a constant high flow rate tends to increase the power consumption of the sensing setup. Thus, despite the present work employing one of the lowest flow rates, the sensing performance registered enhances many other nanomaterials. Similarly, the present work reports one of the lowest exposure times associated with the overall percentage of responses registered.

Table 1. Comparison of the sensing performances to detect DMMP at room temperature employing different carbon-based nanomaterials. ND: information not disponible. SWCNTs and MWCNTs: (single-walled) and (multi-walled) carbon nanotubes. PDLC: polymer-dispersed liquid crystal.

Nanomaterial	Response (%) / Concentration (ppm)	Flow rate (mL/min)	Exposure time (s)	DMMP concentration (ppm) range tested	Ref

$Cs_3Cu_2Br_5$/Graphene	10.2 % / 2.1 ppm	100	300	0.6 - 2.1	This work
$Cs_2AgBiBr_6$/Graphene	2.6 % / 2.1 ppm	100	300	0.6 - 2.1	This work
Graphene	1.35 % / 2.1 ppm	100	300	0.6 - 2.1	This work
p-phenylenediamine rGO	8 % / 20 ppm	1000	1080	5 - 80	[24]
cobalt phthalocyanine /Graphene	9.3 % / 20 ppm	ND	600	0.5 - 100	[25]
Porous graphene multilayer	8.95 % / 50 ppm	1000	240	1 - 50	[38]
SWCNTs	5 % / 25 ppm	ND	1200	25 - 50	[39]
PDLC/CNTs	62.5 % / 250 ppm	ND	300	5 - 250	[40]
Mo_6/Graphene	5.5 % / 1.1 ppm	100	300	0.6 - 2.1	[41]
PPy/rGO	12.9 % / 100 ppm	1000	43	5 - 100	[42]
Functionalized MWCNTs	0.8 % / 100 ppm	ND	30	5 - 100	[43]

Additionally, to assess the potential applicability of the developed nanohybrids in real-world scenarios, the limit of detection (LOD) and limit of quantification (LOQ) should be determined using the following equations:

$LOD = 3S_a/b$

$LOQ = 10S_a/b$

Here, S_a and b represent the standard deviation of y-intercepts and the slope of the fitting, respectively. It has been considered the lowest concentration range tested for performing the linear fitting, ranging from 600 ppb to 1.6 ppm. Table S1 summarizes the linear regression equations obtained and the coefficients of determination. Considering that $Cs_3Cu_2Br_5$ NCs decorating graphene shows the highest sensing performance, the calculated LOD and LOQ are 305 and 1019 ppb of DMMP. These results constitute the first successful detection of a simulant of a chemical nerve agent using halide perovskites. However, it is worth mentioning that the accuracy of these results would probably influenced by humidity, a major interferent in gas sensing [44]. In this context, several studies have shown that some strategies, such as incorporating humidity filters, can effectively mitigate the interfering effects [45,46]. Besides, further optimization of the experimental conditions may lead to more accurate readouts and, hence, potentially lowering the limits obtained.

Sensing mechanism

DMMP is a well-known electron donor molecule [47], and its adsorption on the sensor surface induces an electron transfer to the defects of the NCs. It

has been demonstrated that these defects induce electronic states within the bandgap, which act as trapping states for charge carriers [48]. This trapping can form self-trapped excitons, which can eventually dissociate into free charges. As a result, these charges generated at perovskite NCs are transferred to the graphene sheets, leading to a decrease in hole concentration (Figure 5). Notably, the hybrids present a typical p-type semiconductor behavior since the resistance of the sensitive films increases upon interaction with an electron donor gas. Following partial oxidation, a small number of oxygenated groups are formed, graphene presents a subtle p-type semiconductor behavior, meaning that holes become the dominant carriers. Additionally, carrier mobility can also be affected, altering the effective carrier density [49]. In any case, considering that perovskite nanocrystals present and ambipolar behavior, the films overall act as p-type semiconductors owing to the prevalence of graphene [50].

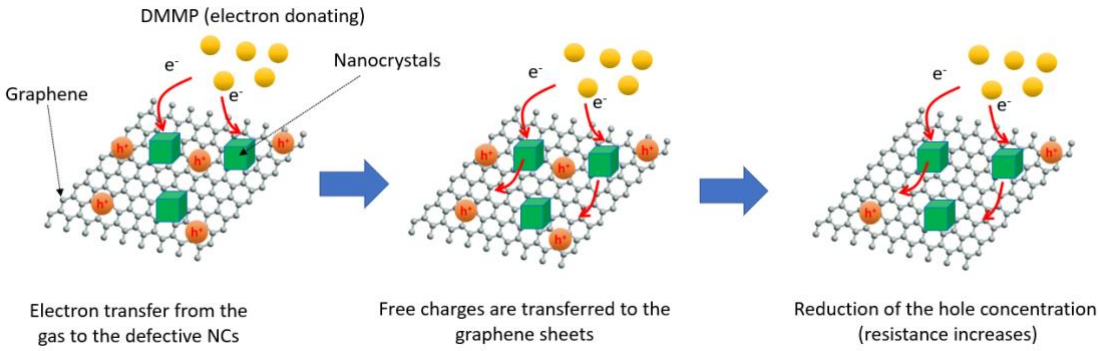

Figure 5. Sensing mechanism of DMMP employing graphene decorated with lead-free perovskite nanocrystals.

The sensitivity observed in both nanohybrids is largely attributed to the perovskite nanocrystals. In essence, while a weak interaction between DMMP and graphene cannot be entirely ruled out, the electrical responses primarily stem from the interaction of lead-free perovskites with the analyte, as observed in analogous previous works [51]. When the DMMP interact with sensitive films, negative carriers likely accumulate at the perovskite nanocrystals. This prompts graphene to transfer positive carriers to the nanocrystals, resulting in an excess of electrons in the graphene layers. Consequently, resistivity increases, given that electrons are not the majority charge carriers in p-type semiconductors.

The noteworthy sensing performance achieved when using lead-free perovskites can be partially attributed to the quantum confinement effect

stemming from the nanocrystal shape [52,53]. This confined structure provides an efficient radiative recombination of carriers [54], contributing to an enhanced overall sensing performance. Besides, perovskite nanocrystals tend to form self-trapped excitons, increasing their interaction with gaseous analytes [55]. But not limited to this, the high and efficient carriers' mobility of graphene likely facilitates the interaction of DMMP with lead-free perovskites [56].

Nevertheless, a significant difference in the sensing performance depending on the composition of the lead-free perovskite employed was observed. The results obtained with $Cs_3Cu_2Br_5$ NCs surpass those recorded for $Cs_2AgBiBr_6$ NCs across various sensing parameters like response, sensitivity, and reversibility. This discrepancy is likely rooted in the semiconductor type, as $Cs_3Cu_2Br_5$ and $Cs_2AgBiBr_6$ present direct and indirect bandgaps, respectively [51]. Consequently, $Cs_3Cu_2Br_5$, with its direct bandgap, exhibits superior sensing performance, benefiting from advantages such as the presence of radiative self-trapped excitons with moderate strength of exciton-phonon coupling and a more efficient recombination of carriers [57,58].

Conclusions

The graphene decoration with lead-free perovskite nanocrystals, particularly $Cs_3Cu_2Br_5$, have demonstrated superior properties to detect DMMP, a simulant for chemical nerve agents. The LOD and LOQ are estimated as 55 ppb and 182 ppb, respectively, outperforming the sensing performance of other carbon-based hybrids. Besides, the $Cs_3Cu_2Br_5$ presents better reversibility than $Cs_2AgBiBr_6$, which probably lead to a better repeatability and long-term stability. It is worth noting that the DMMP was performed at ambient temperature, resulting to inexpensive sensing devices with minimal power consumption. The lead-free nature of the synthesized perovskites significantly enhances safety while maintaining excellent sensing properties, paving the way for the development of advanced gas detection systems for chemical defense and safety applications.

Acknowledgements

J.C.-C. is supported by the Marie Skłodowska-Curie Postdoctoral Fellowship (Horizon Europe Programme) under grant agreement No. 101066282 "GREBOS". E.L. is supported by the Catalan Institute for Advanced Studies

(ICREA) via the 2018 Edition of the ICREA Academia Award. This work was supported in part by the Marie Skłodowska-Curie Action (MSCA) Research and in part by the Innovation Staff Exchange (RISE) under Grant no. H2020-MSCA-RISE-2018-823895 “SENSOFT”. This research was also funded by the ITQ though the project PID2021-123163OB-I00 funded by MCIN/AEI/10.13039/501100011033/ and FEDER A way of making Europe and Severo Ochoa centre of excellence program (CEX2021-001230-S).

References

[1] Chauhan, S.; Chauhan, S.; D’Cruz, R.; Faruqi, S.; Singh, K.K.; Varma, S.; Singh, M.; Karthik, V. Chemical Warfare Agents. *Environ. Toxicol. Pharmacol.*, **2008**, *26*, 113–122.

[2] Sidell, F.R.; Borak, J. Chemical Warfare Agents: II. Nerve Agents. *Ann. Emerg. Med.*, **1992**, *21*, 865–871.

[3] Zheng, Q.; Fu, Y.C.; Xu, J.Q. Advances in the Chemical Sensors for the Detection of DMMP — A Simulant for Nerve Agent Sarin. *Procedia Eng.*, **2010**, *7*, 179–184.

[4] Bartelt-Hunt, S.L.; Knappe, D.R.U.; Barlaz, M.A. A Review of Chemical Warfare Agent Simulants for the Study of Environmental Behavior. *Crit. Rev. Environ. Sci. Technol.*, **2008**, *38*, 112–136.

[5] Mitchell, B.L.; Billingsley, B.G.; Logue, B.A. Rapid Quantification of Dimethyl Methylphosphonate from Activated Carbon Particles by Static Headspace Gas Chromatography Mass Spectrometry. *J. Chromatogr. A*, **2013**, *1293*, 120–125.

[6] Hoggard, J.C.; Wahl, J.H.; Synovec, R.E.; Mong, G.M.; Fraga, C.G. Impurity Profiling of a Chemical Weapon Precursor for Possible Forensic Signatures by Comprehensive Two-Dimensional Gas Chromatography/Mass Spectrometry and Chemometrics. *Anal. Chem.*, **2009**, *82*, 689–698.

[7] Witkiewicz, Z.; Jasek, K.; Grabka, M. Semiconductor Gas Sensors for Detecting Chemical Warfare Agents and Their Simulants. *Sensors 2023, Vol. 23, Page 3272*, **2023**, *23*, 3272.

[8] Khan, M.A.K.; Long, Y.T.; Schatte, G.; Kraatz, H.B. Surface Studies of Aminoferrocene Derivatives on Gold: Electrochemical Sensors for Chemical Warfare Agents. *Anal. Chem.*, **2007**, *79*, 2877–2884.

[9] Grabka, M.; Witkiewicz, Z.; Jasek, K.; Piwowarski, K. Acoustic Wave

Sensors for Detection of Blister Chemical Warfare Agents and Their Simulants. *Sensors 2022, Vol. 22, Page 5607*, **2022**, *22*, 5607.

[10] Davidson, C.E.; Dixon, M.M.; Williams, B.R.; Kilper, G.K.; Lim, S.H.; Martino, R.A.; Rhodes, P.; Hulet, M.S.; Miles, R.W.; Samuels, A.C.; Emanuel, P.A.; Miklos, A.E. Detection of Chemical Warfare Agents by Colorimetric Sensor Arrays. *ACS Sensors*, **2020**, *5*, 1102–1109.

[11] Wiederoder, M.S.; Nallon, E.C.; Weiss, M.; McGraw, S.K.; Schnee, V.P.; Bright, C.J.; Polcha, M.P.; Paffenroth, R.; Uzarski, J.R. Graphene Nanoplatelet-Polymer Chemiresistive Sensor Arrays for the Detection and Discrimination of Chemical Warfare Agent Simulants. *ACS Sensors*, **2017**, *2*, 1669–1678.

[12] Freris, N.M.; Kowshik, H.; Kumar, P.R. Fundamentals of Large Sensor Networks: Connectivity, Capacity, Clocks, and Computation. *Proc. IEEE*, **2010**, *98*, 1828–1846.

[13] Majhi, S.M.; Mirzaei, A.; Kim, H.W.; Kim, S.S.; Kim, T.W. Recent Advances in Energy-Saving Chemiresistive Gas Sensors: A Review. *Nano Energy*, **2021**, *79*, 105369.

[14] Jian, Y.; Hu, W.; Zhao, Z.; Cheng, P.; Haick, H.; Yao, M.; Wu, W. Gas Sensors Based on Chemi-Resistive Hybrid Functional Nanomaterials. *Nano-Micro Lett.*, **2020**, *12*, 1–43.

[15] Yang, Z.; Zhao, L.; Zhang, Y.; Xing, Y.; Fei, T.; Liu, S.; Zhang, T. DMMP Sensors Based on Au-SnO2 Hybrids Prepared through Colloidal Assembly Approach: Gas Sensing Performances and Mechanism Study. *Sensors Actuators B Chem.*, **2022**, *369*, 132278.

[16] Alali, K.T.; Liu, J.; Yu, J.; Moharram, D.; Chen, R.; Zhang, H.; Liu, Q.; Zhang, M.; Wang, J. HFIP-Functionalized Electrospun WO3 Hollow Nanofibers/RGO as an Efficient Double Layer Sensing Material for Dimethyl Methylphosphonate Gas under UV-Light Irradiation. *J. Alloys Compd.*, **2020**, *832*, 154999.

[17] Yoo, R.; Yoo, S.; Lee, D.; Kim, J.; Cho, S.; Lee, W. Highly Selective Detection of Dimethyl Methylphosphonate (DMMP) Using CuO Nanoparticles /ZnO Flowers Heterojunction. *Sensors Actuators B Chem.*, **2017**, *240*, 1099–1105.

[18] Alali, K.T.; Liu, J.; Chen, R.; Liu, Q.; Zhang, H.; Li, J.; Hou, J.; Li, R.; Wang, J. HFIP-Functionalized Co3O4 Micro-Nano-Octahedra/RGO as a Double-Layer Sensing Material for Chemical Warfare Agents.

Chem. – A Eur. J., **2019**, *25*, 11892–11902.

[19] Raya, I.; Kzar, H.H.; Mahmoud, Z.H.; Al Ayub Ahmed, A.; Ibatova, A.Z.; Kianfar, E. A Review of Gas Sensors Based on Carbon Nanomaterial. *Carbon Lett.*, **2022**, *32*, 339–364.

[20] Bannov, A.G.; Popov, M. V.; Brester, A.E.; Kurmashov, P.B. Recent Advances in Ammonia Gas Sensors Based on Carbon Nanomaterials. *Micromachines 2021, Vol. 12, Page 186*, **2021**, *12*, 186.

[21] Shaalan, N.M.; Ahmed, F.; Kumar, S.; Melaibari, A.; Hasan, P.M.Z.; Aljaafari, A. Monitoring Food Spoilage Based on a Defect-Induced Multiwall Carbon Nanotube Sensor at Room Temperature: Preventing Food Waste. *ACS Omega*, **2020**, *5*, 30531–30537.

[22] Lee, S.W.; Lee, W.; Hong, Y.; Lee, G.; Yoon, D.S. Recent Advances in Carbon Material-Based NO2 Gas Sensors. *Sensors Actuators B Chem.*, **2018**, *255*, 1788–1804.

[23] Kim, Y.T.; Lee, S.; Park, S.; Lee, C.Y. Graphene Chemiresistors Modified with Functionalized Triphenylene for Highly Sensitive and Selective Detection of Dimethyl Methylphosphonate. *RSC Adv.*, **2019**, *9*, 33976–33980.

[24] Hu, N.; Wang, Y.; Chai, J.; Gao, R.; Yang, Z.; Kong, E.S.W.; Zhang, Y. Gas Sensor Based on P-Phenylenediamine Reduced Graphene Oxide. *Sensors Actuators B Chem.*, **2012**, *163*, 107–114.

[25] Jiang, W.; Jiang, M.; Wang, T.; Chen, X.; Zeng, M.; Yang, J.; Zhou, Z.; Hu, N.; Su, Y.; Yang, Z. Room Temperature DMMP Gas Sensing Based on Cobalt Phthalocyanine Derivative/Graphene Quantum Dot Hybrid Materials. *RSC Adv.*, **2021**, *11*, 14805–14813.

[26] Casanova-Chafer, J.; Blanch, X.; Llobet, E. Polypyrrole Nanoparticles Suspended on Graphene for the Detection of Simulant Chemical Warfare Agents. *IEEE Sensors Lett.*, **2023**, *7*.

[27] Park, J.; Kim, J.; Kim, K.; Kim, S.Y.; Cheong, W.H.; Park, K.; Song, J.H.; Namgoong, G.; Kim, J.J.; Heo, J.; Bien, F.; Park, J.U. Wearable, Wireless Gas Sensors Using Highly Stretchable and Transparent Structures of Nanowires and Graphene. *Nanoscale*, **2016**, *8*, 10591–10597.

[28] Yang, Z.; Zhao, L.; Zhang, Y.; Xing, Y.; Wei, Z.; Xin, C.; Fei, T.; Liu, S.; Zhang, T. Isolated Cu-N5 Sites Engineered Polypyrrole-Reduced Graphene Oxide Hybrids for Enhancing Room-Temperature DMMP

Sensing. *Sensors Actuators B Chem.*, **2023**, *385*, 133671.

[29] Li, Y.; Vashishtha, P.; Zhou, Z.; Li, Z.; Shivarudraiah, S.B.; Ma, C.; Liu, J.; Wong, K.S.; Su, H.; Halpert, J.E. Room Temperature Synthesis of Stable, Printable Cs3Cu2X5(X = I, Br/I, Br, Br/Cl, Cl) Colloidal Nanocrystals with Near-Unity Quantum Yield Green Emitters (X = Cl). *Chem. Mater.*, **2020**, *32*, 5515–5524.

[30] Zhou, L.; Xu, Y.F.; Chen, B.X.; Kuang, D. Bin; Su, C.Y. Synthesis and Photocatalytic Application of Stable Lead-Free Cs2AgBiBr6 Perovskite Nanocrystals. *Small*, **2018**, *14*, 1703762.

[31] Yu, W.; Li, F.; Huang, T.; Li, W.; Wu, T. Go beyond the Limit: Rationally Designed Mixed-Dimensional Perovskite/Semiconductor Heterostructures and Their Applications. *Innov.*, **2023**, *4*, 100363.

[32] Zhan, J.; Lei, Z.; Zhang, Y. Non-Covalent Interactions of Graphene Surface: Mechanisms and Applications. *Chem*, **2022**, *8*, 947–979.

[33] Malard, L.M.; Pimenta, M.A.; Dresselhaus, G.; Dresselhaus, M.S. Raman Spectroscopy in Graphene. *Phys. Rep.*, **2009**, *473*, 51–87.

[34] Casanova-Chafer, J.; Garcia-Aboal, R.; Atienzar, P.; Feliz, M.; Llobet, E. Octahedral Molybdenum Iodide Clusters Supported on Graphene for Resistive and Optical Gas Sensing. *ACS Appl. Mater. Interfaces*, **2022**, *14*, 23.

[35] Casanova-Chafer, J.; Garcia-Aboal, R.; Atienzar, P.; Llobet, E. The Role of Anions and Cations in the Gas Sensing Mechanisms of Graphene Decorated with Lead Halide Perovskite Nanocrystals. *Chem. Commun.*, **2020**, *56*, 8956–8959.

[36] Yang, B.; Chen, J.; Yang, S.; Hong, F.; Sun, L.; Han, P.; Pullerits, T.; Deng, W.; Han, K. Lead-Free Silver-Bismuth Halide Double Perovskite Nanocrystals. *Angew. Chemie Int. Ed.*, **2018**, *57*, 5359–5363.

[37] Casanova-Chafer, J.; Umek, P.; Acosta, S.; Bittencourt, C.; Llobet, E. Graphene Loading with Polypyrrole Nanoparticles for Trace-Level Detection of Ammonia at Room Temperature. *ACS Appl. Mater. Interfaces*, **2021**, *13*, 40909–40921.

[38] Wang, Y.; Yang, M.; Liu, W.; Dong, L.; Chen, D.; Peng, C. Gas Sensors Based on Assembled Porous Graphene Multilayer Frameworks for DMMP Detection. *J. Mater. Chem. C*, **2019**, *7*, 9248–9256.

[39] Cattanach, K.; Kulkarni, R.D.; Kozlov, M.; Manohar, S.K. Flexible

Carbon Nanotube Sensors for Nerve Agent Simulants. *Nanotechnology*, **2006**, *17*, 4123.

[40] Lai, Y.T.; Kuo, J.C.; Yang, Y.J. Polymer-Dispersed Liquid Crystal Doped with Carbon Nanotubes for Dimethyl Methylphosphonate Vapor-Sensing Application. *Appl. Phys. Lett.*, **2013**, *102*.

[41] Casanova-Chafer, J.; Blanch, X.; Moreno, A.; Garcia-Aboal, R.; Atienzar, P.; Llobet, E.; Feliz, M. Graphene Based Mo6 Cluster Hybrid for Detecting Simulant Nerve Agent DMMP. *Sens. Bio-Sensing Res.*, **2024**, *43*, 100603.

[42] Yang, Z.; Zhang, Y.; Gao, S.; Zhao, L.; Fei, T.; Liu, S.; Zhang, T. Hydrogen Bonds-Induced Room-Temperature Detection of DMMP Based on Polypyrrole-Reduced Graphene Oxide Hybrids. *Sensors Actuators B Chem.*, **2021**, *346*, 130518.

[43] Saetia, K.; Schnorr, J.M.; Mannarino, M.M.; Kim, S.Y.; Rutledge, G.C.; Swager, T.M.; Hammond, P.T. Spray-Layer-by-Layer Carbon Nanotube/Electrospun Fiber Electrodes for Flexible Chemiresistive Sensor Applications. *Adv. Funct. Mater.*, **2014**, *24*, 492–502.

[44] Samad, A.; Nuñez, D.R.O.; Castillo, G.C.S.; Laquai, B.; Vogt, U. Effect of Relative Humidity and Air Temperature on the Results Obtained from Low-Cost Gas Sensors for Ambient Air Quality Measurements. *Sensors*, **2020**, *20*, 5175.

[45] Mahdavi, H.; Rahbarpour, S.; Hosseini-Golgoo, S.M.; Jamaati, H. Reducing the Destructive Effect of Ambient Humidity Variations on Gas Detection Capability of a Temperature Modulated Gas Sensor by Calcium Chloride. *Sensors Actuators B Chem.*, **2021**, *331*, 129091.

[46] Recent, Y.; Kulinich, S.; Wang, Y.; Zhou, Y. Recent Progress on Anti-Humidity Strategies of Chemiresistive Gas Sensors. *Materials (Basel).*, **2022**, *15*, 8728.

[47] Alizadeh, T.; Soltani, L.H. Reduced Graphene Oxide-Based Gas Sensor Array for Pattern Recognition of DMMP Vapor. *Sensors Actuators B Chem.*, **2016**, *234*, 361–370.

[48] Lian, L.; Zheng, M.; Zhang, P.; Zheng, Z.; Du, K.; Lei, W.; Gao, J.; Niu, G.; Zhang, D.; Zhai, T.; Jin, S.; Tang, J.; Zhang, X.; Zhang, J. Photophysics in Cs3Cu2X5(X = Cl, Br, or I): Highly Luminescent Self-Trapped Excitons from Local Structure Symmetrization. *Chem. Mater.*, **2020**, *32*, 3462–3468.

[49] Georgakilas, V.; Otyepka, M.; Bourlinos, A.B.; Chandra, V.; Kim, N.; Kemp, K.C.; Hobza, P.; Zboril, R.; Kim, K.S. Functionalization of Graphene: Covalent and Non-Covalent Approaches, Derivatives and Applications. *Chem. Rev.*, **2012**, *112*, 6156–6214.

[50] Casanova-Cháfer, J.; García-Aboal, R.; Atienzar, P.; Llobet, E. Gas Sensing Properties of Perovskite Decorated Graphene at Room Temperature. *Sensors*, **2019**, *19*, 4563.

[51] Casanova-Chafer, J.; Garcia-Aboal, R.; Atienzar, P.; Llobet, E. Unraveling the Gas-Sensing Mechanisms of Lead-Free Perovskites Supported on Graphene. *ACS Sensors*, **2022**, *7*, 3753–3763.

[52] Tyagi, P.; Arveson, S.M.; Tisdale, W.A. Colloidal Organohalide Perovskite Nanoplatelets Exhibiting Quantum Confinement. *J. Phys. Chem. Lett.*, **2015**, *6*, 1911–1916.

[53] Yang, X.; Zhang, X.; Deng, J.; Chu, Z.; Jiang, Q.; Meng, J.; Wang, P.; Zhang, L.; Yin, Z.; You, J. Efficient Green Light-Emitting Diodes Based on Quasi-Two-Dimensional Composition and Phase Engineered Perovskite with Surface Passivation. *Nat. Commun.*, **2018**, *9*, 1–8.

[54] Saparov, B.; Mitzi, D.B. Organic-Inorganic Perovskites: Structural Versatility for Functional Materials Design. *Chem. Rev.*, **2016**, *116*, 4558–4596.

[55] Hu, T.; Smith, M.D.; Dohner, E.R.; Sher, M.J.; Wu, X.; Trinh, M.T.; Fisher, A.; Corbett, J.; Zhu, X.Y.; Karunadasa, H.I.; Lindenberg, A.M. Mechanism for Broadband White-Light Emission from Two-Dimensional (110) Hybrid Perovskites. *J. Phys. Chem. Lett.*, **2016**, *7*, 2258–2263.

[56] Cooper, D.R.; D'Anjou, B.; Ghattamaneni, N.; Harack, B.; Hilke, M.; Horth, A.; Majlis, N.; Massicotte, M.; Vandsburger, L.; Whiteway, E.; Yu, V. Experimental Review of Graphene. *ISRN Condens. Matter Phys.*, **2012**, *2012*, 1–56.

[57] Kim, H.; Hunger, J.; Cánovas, E.; Karakus, M.; Mics, Z.; Grechko, M.; Turchinovich, D.; Parekh, S.H.; Bonn, M. Direct Observation of Mode-Specific Phonon-Band Gap Coupling in Methylammonium Lead Halide Perovskites. *Nat. Commun.*, **2017**, *8*, 1–9.

[58] Li, X.; Gao, X.; Zhang, X.; Shen, X.; Lu, M.; Wu, J.; Shi, Z.; Colvin, V.L.; Hu, J.; Bai, X.; Yu, W.W.; Zhang, Y. Lead-Free Halide Perovskites for Light Emission: Recent Advances and Perspectives. *Adv. Sci.*, **2021**, *8*,

2003334.

for TOC only

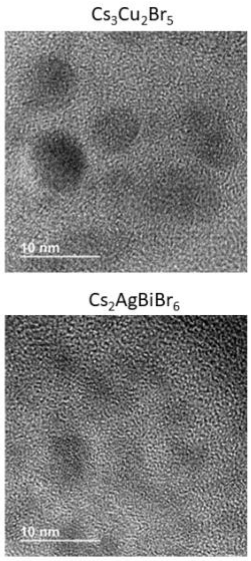
$Cs_3Cu_2Br_5$
10 nm
$Cs_2AgBiBr_6$
10 nm

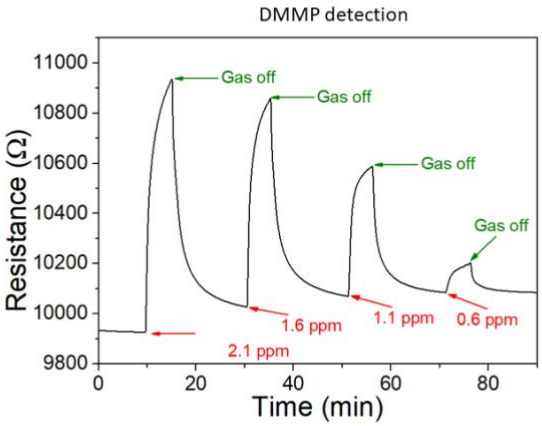
DMMP detection
Resistance (Ω)
Time (min)
11000
10800
10600
10400
10200
10000
9800
0
20
40
60
80
Gas off
Gas off
Gas off
Gas off
2.1 ppm
1.6 ppm
1.1 ppm
0.6 ppm